J Mater Sci (2011) 46:5466–5476
DOI 10.1007/s10853-011-5489-5

# Role of doping-induced photochemical and microstructural properties in the photocatalytic activity of $InVO_4$ for splitting of water

**K. Rakesh · S. Khaire · D. Bhange · P. Dhanasekaran · S. S. Deshpande · S. V. Awate · N. M. Gupta**

Received: 23 December 2010 / Accepted: 18 March 2011 / Published online: 30 March 2011


**Abstract** We report in this paper on microstructural, optical and photocatalytic properties of single-phase indium orthovanadates, as a function of doping at lattice sites. The UV–visible spectra of these samples exhibited intense UV-region bands at 250 and 350 nm, besides broad absorption band in visible region (350–700 nm). The wavelength at absorption edge and the intensity of visible absorption showed considerable increase on doping of an impurity, particularly at V or O lattice sites. Also, the samples gave rise to blue-green photoluminescence emission, with overriding bands at ca. 420, 450, 460 and 485 nm, on excitation at 240–420 nm wavelengths. The intensity of these fluorescence bands varied with excitation wavelength and impurity content of a sample. In deviation with several earlier studies, only oxygen and no hydrogen were produced during photocatalytic splitting of water, in the experiments conducted under visible light (>395 nm) and at a pH of ~6.5. The $O_2$ yield depended on the dispersed metal co-catalyst, impurity content and the addition of methanol as sacrificial reagent. On the other hand, small quantities of hydrogen and no oxygen were evolved on UV-irradiation of pure water using metal/$InVO_4$. These results are ascribed to flat band potentials and the doping-induced inter-band donor and acceptor charge trapping states of $InVO_4$, the presence of which is revealed by XRD, luminescence and XPS studies. Our study also confirms that the onset of absorption edge may not necessarily correspond to band-to-band energy gap of a semiconducting material. This accounts for some anomalous band gap energies reported earlier for $InVO_4$.

K. Rakesh · S. Khaire · D. Bhange · P. Dhanasekaran · S. S. Deshpande · S. V. Awate · N. M. Gupta (✉)
Catalysis Division, National Chemical Laboratory, Dr. Homi Bhabha Road, Pune 411008, India
e-mail: nm.gupta@ncl.res.in

## Introduction

The semiconductor-mediated and solar radiation-induced production of hydrogen by way of photocatalytic splitting of water continues to receive wide attention, because of its strategic importance in the worldwide search for alternative fuels [1]. As is well documented [2], an efficient water splitting photocatalyst needs to fulfil several criteria, such as: absorption in visible region with a band gap greater than the theoretical dissociation energy of water molecules (1.23 eV); conduction band potential more negative than $H^+/H_2$ (0 V vs SHE at pH 0); valence band potential more positive than $O_2/H_2O$ (1.23 V vs. SHE at pH 0); high chemical stability in aqueous medium against photocorrosion; and the controlled recombination of charge carriers to achieve better quantum yields. A large number of semiconducting mixed metal oxides have accordingly been synthesized to serve as the viable water splitting photocatalysts [3–5].

The metal orthovanadates are reported to be the potential visible light sensitive photocatalysts because of their suitable band gap and the chemical stability. Indium vanadate ($InVO_4$), in particular, is found to be active for the production of hydrogen from splitting of water, both under UV as well as visible light irradiation [6–8]. These photocatalytic properties have been attributed to a small band gap (~2.0 eV) and the open crystal structure of $InVO_4$. Also, the photocatalytic activity of $InVO_4$ to produce $H_2$ from water splitting is found to depend upon sample preparation method. Thus, a mesoporous sample of indium vanadate, synthesized by a template-directing self-assembly method, and a nanostructured orthorhombic $InVO_4$ sample prepared

by using an amorphous heteronuclear complex as precursor are found to exhibit better photocatalytic activity for production of $H_2$ from water splitting, compared to the samples prepared by ceramic route [8, 9]. Discrepant results have also been reported in regards to the photocatalytic properties of indium vanadate. Thus, whereas several research groups have observed hydrogen evolution from visible-light-induced photocatalytic splitting of water using $InVO_4$ and $NiO/InVO_4$ [6–8], no hydrogen was produced using $InVO_4$ as well as an $InVO_4$:$TlVO_4$ composite photocatalyst in a recent photoelectrochemical study of Butcher and Gewirth [10]. Also, a large variation in the band gap energy (1.8–3.5 eV), estimated both experimentally and theoretically, has been reported earlier for $InVO_4$ [6–14], as is summarized in Table 2.

The aim of present study was to understand how the water splitting photocatalytic activity of indium orthovanadate may depend upon its physicochemical, microstructural and optical properties. To achieve this objective, indium vanadate samples, having substitution at different lattice sites, were synthesized. A dopant was chosen randomly on the basis of its electronegativity and ionic radius, i.e. Ti at V sites ($InV_{1-x}Ti_xO_4$), Sr at In sites ($In_{1-x}Sr_xVO_4$) and the traces of S at the oxygen sites. Different metals, e.g. Pt, Au and Ni, were dispersed over the sample surface for a loading of $\sim$0.7 wt%, so as to serve as a co-catalyst. Whereas Pt and Au were loaded in their zerovalent state, nickel was deposited in an oxide form in view of the high activity reported for NiO co-catalyst [6]. The samples were characterized systematically for their morphological, structural and optical properties. The photocatalytic activity was monitored for the splitting of water under visible light as well as UV radiation.

## Experimental methods

### Synthesis

Indium vanadate samples, with the nominal compositions of $InV_{1-x}Ti_xO_4$ ($0.0 \leq x \leq 0.1$) and $In_xSr_{1-x}VO_4$ ($0.0 \leq x \leq 0.1$), were prepared by solid-state reaction method. Thus, for the preparation of a typical Ti-doped sample, a stoichiometric mixture of $In_2O_3$ (Aldrich, 99.9% purity), $TiO_2$ (Merck, anatase, 99.9% purity) and $V_2O_5$ (Merck, AR grade) were ground mechanically for $\sim$12 h and then palletized into 24 mm diameter discs. These pellets were heated in air in three temperature steps, i.e. 720 K (8 h), 873 K (8–10 h) and finally 1073 K (8 h), with in-between grindings to ensure the phase purity and the completion of the reaction. The Sr-doped samples were synthesized by following similar calcinations protocol, and the stoichiometric amounts of $In_2O_3$ and $SrCO_3$ (Sarabhai Chemicals, 99.5% purity) were employed for this purpose. The actual amount of Sr or Ti doped was found to be short by ca. 5–10% in some of the samples, and the value of $x$ for different samples, as estimated by ICP analysis, is included in Table 1. A few sulphur-doped samples were also prepared by following an earlier reported procedure [15]. For this purpose, as-synthesized $InVO_4$ and thiourea powders were ball-milled for $\sim$2 h. The starting mol ratio of these two ingredients was 1:1 and 1.025 in the two representative S-doped samples prepared in this study. The samples were then heated under vacuum ($\sim 10^{-2}$ Torr), at a temperature of 925 K. Much of the thiourea was removed during this heating, leaving very small amount of sulphur in the sample. The approximate S-substitution (with respect to oxygen), in the two samples prepared this way, was estimated to be ca. 0.3 and 0.02 atom% by EDAX measurements. For the sake of convenience, the two S-doped samples, i.e. $InVO_{3.997}S_{0.003}$ and $InVO_{3.9998}$ $S_{0.0002}$, are designated in the text as $InVO_{1-y}S_y$ and $InVO_{1-z}S_z$, respectively.

The samples described above were impregnated with 1 wt% of a metal co-catalyst, such as Pt, Ni or Au. For this purpose, a sample soaked in required amount of metal salt solution was dried at 370 K, followed by heating in air at 625 or 525 K (4 h). Pt and Au were converted to their metallic state on the exposure (10–12 h) to UV radiation from a 400 W mercury vapour lamp. The ICP analysis revealed that the final metal content in the as-synthesized samples varied from 0.7 to 0.8 wt%.

**Table 1** Physical characteristics of doped indium orthovanadate samples

| Sample | Actual $x$-value[a] | Surface area[b] ($m^2g^{-1}$), ±5% | Absorption edge energy gap[c] eV ± 0.05 |
|---|---|---|---|
| $InVO_4$ | – | 4.0 | 2.2 |
| $InV_{0.98}Ti_{0.02}O_4$ | 0.014 | 15.0 | 2.0 |
| $InV_{0.95}Ti_{0.05}O_4$ | 0.051 | 7.0 | 1.9 |
| $InV_{0.9}Ti_{0.1}O_4$ | 0.086 | 5.0 | 1.7 |
| $In_{0.98}$ $Sr_{0.02}VO_4$ | 0.018 | 10.0 | 2.2 |
| $In_{0.95}$ $Sr_{0.05}VO_4$ | 0.049 | 8.0 | 2.1 |
| $In_{0.9}Sr_{0.1}VO_4$ | 0.092 | 5.0 | 2.0 |
| In $VO_{1-y}S_y$ | – | 5.0 | – |

[a] By ICP analysis

[b] By $N_2$ adsorption at 77 K

[c] From the wavelength at onset of absorption edge in DR UV–visible spectra

### Catalyst characterization

The powder X-ray diffraction patterns of calcined samples were collected in Bragg–Brentano geometry on a Rigaku-Miniflex diffractometer. A Ni filter was utilized to suppress $CuK_\beta$ radiation. The patterns were collected in a continuous scan mode in $2\theta$ range 10–80° and with the step size of 0.02°. Goniometer zero correction was applied with respect to XRD scan of a Si standard. The diffraction patterns were analyzed by Rietveld refinement using the X'Pert plus package. Starting atomic coordinates and the thermal parameters for parent $InVO_4$ phase of orthorhombic symmetry (space group *Cmcm*) were taken from the X-ray crystal structure of $InVO_4$, as reported by Touboul and Toledano [16]. The average size of crystallites in different samples was estimated by using Scherer equation [17].

The UV–vis diffuse reflectance spectra were recorded on Perkin–Elmer (Lambda 650) spectrophotometer, using barium sulphate for reference. Following a widely adopted procedure, the inflection point of band edge in UV–vis spectra was used for the estimation of band gap energy. The flat band potentials were calculated by using the following relationship between atomic electronegativity, conduction band potential and the electron affinity of a metal oxide semiconductor [18, 19].

$$E_c = E_A - 0.5 \times E_{gap} \quad (1)$$

where $E_c$ the conduction band potential (with respect to absolute vacuum level), $E_A$ the electron affinity = Electronegativity ($\chi$), $E_{gap}$ the valence band to conduction band transition energy, referred to as band-to-band gap.

For $InVO_4$, $\chi_{InVO_4} = \left[\chi_{In} + \chi_V + \chi_O^4\right]^{1/6}$.

Photoluminescence spectra were recorded on Perkin-Elmer LS 50 B Luminescence spectrometer on excitation at different wavelengths. An ultrasonically dispersed aqueous suspension of a photocatalyst sample was utilized for this purpose. X-ray photoelectron spectroscopy (XPS) analysis was conducted on VG Scientific ESCA-3000 unit, equipped with $MgK_\alpha$ X-ray (1253.6 eV) source and operating at 150 W under ultrahigh vacuum. The energy calibration was accomplished with reference to binding energy of an extraneous C1s signal (284.6 eV). The texture of the sample grains was monitored by collecting SEM images on a dual beam scanning electron microscope (FEI company, model Quanta 200 3D, tungsten filament). For these SEM studies, a drop of ultrasonicated catalyst suspension in isopropyl alcohol was placed on a sample holder and then dried under an infrared lamp before being mounted in the microscope chamber. The transmission electron microscopy (TEM) pictures and the selected area electron diffraction (SAED) images were taken on Tecnai (model-F30) 300 kV field emission gun (FEG) high resolution transmission electron microscope, supplied by FEI Company (Netherlands).

### Photocatalytic activity

The photocatalytic activity of different samples was monitored under static condition for the photosplitting of $H_2O$ under visible light. The reaction was carried out at normal pressure using a quartz photo reactor of ca. 100 mL capacity, equipped with a port for the withdrawal of gas samples at regular intervals. For each experiment, about 200 mg of a fresh catalyst sample was dispersed well in 10 mL water by ultrasonication and the cell was then purged with nitrogen. A 300 W Xenon arc lamp (model XDS-301S, M. Watanabe & Co, Japan, irradiance 100,000 Lx), coupled with a 395 nm cut-off filter of 2 mm thickness (CVI Meller Griot CG-GG-395-50), was utilized for visible light irradiation. The light source was positioned vertically at a distance of $\sim$6 cm from the reaction cell and the water column was stirred magnetically. Experiments were carried out without and also in the presence of methanol (5 mL in 10 mL water) as a sacrificial reagent. Most of the experiments were carried out at a solution pH of 6.3–6.5, and the cell attained a maximum temperature of $\sim$310 K during its prolonged irradiation. A few exploratory activity tests at the solution pH of ca. 2 and 14 were also performed. The comparative activity measurements were conducted under UV light also, by utilizing a water-cooled 400 W mercury vapour lamp (emission: 220–400 nm peaking at 260 nm, flux: 24000 lumen), housed in a double-walled quartz vessel. A 250 nm long-pass filter (Asahi Spectra, ZUL-0250) was used to cut off deep UV radiation and the experiments were conducted without adding any sacrificial agent. The reaction products were analyzed on a gas chromatograph (Nucon-5765, India, thermal conductivity detector at 360 K, argon as a carrier gas), equipped with a 2.5 m packed column of molecular sieve-5A. This instrument showed good $H_2$ response to the standard 10–100 μl sample injections for multipoint calibration.

## Results

### Physical and morphological characteristics

$InVO_4$ and corresponding doped samples showed a surface area varying from 2 to 15 $m^2g^{-1}$ (Table 1). The scanning electron microscopic examination revealed the non-uniform morphology of the grains, their cross-sectional size varying from 1 to 4 μm. Some of the large size grains were found to

be agglomerated. Only marginal variation in grain size was noticed in the case of impurity-doped samples. The transmission electron microscopy images showed that the basic crystallites were of polyhedral shape and measured ca. 0.3–1.5 μm in their cross-sectional size, the average crystallite size being ~0.8 μm.

## Powder XRD patterns and Rietveld refinement

*$InV_{1-x}Ti_xO_4$ samples*. Curve (b) in Fig. 1 shows XRD pattern of pure $InVO_4$ and curve (a) is the theoretically simulated spectrum for comparison. The XRD lines in Fig. 1a and b match well with the XRD data for $InVO_4$ having orthorhombic symmetry (*Cmcm* space group), as reported in several publications [7–12, 16, 20]. Curves (c) to (e) in Fig. 1 display the representative powder XRD patterns of $InV_{1-x}Ti_xO_4$ samples, for the values of $x$ varying from 0.02 to 0.1. The complete absence of reflections due to precursor oxides in the XRD patterns in Fig. 1 indicates the completion of the reaction and the formation of a single phase material in each case. Similarly, the Sr-substituted indium vanadates, i.e. $In_{1-x}Sr_xVO_4$ ($0.0 \leq x \leq 0.1$), and also the samples prepared by substitution of sulphur at oxygen sites were found to be isostructural with $InVO_4$ and gave rise to X-ray diffraction patterns similar to those in curves (a) and (b) of Fig. 1. Curves (f) and (g) in Fig. 1 present the representative XRD patterns of $In_{0.9}Sr_{0.1}VO_4$ and $InVO_{1-y}S_y$ photocatalysts, respectively.

A systematic change is noticeable in Fig. 1 in the relative intensity of certain XRD reflections, e.g. the lines at $2\theta$ values 18.56° and 33.01° corresponding to (110) and (112) reflections. Thus, the intensity ratio $I_{(112)}/I_{(110)}$, plotted in Fig. 2 for $InV_{1-x}Ti_xO_4$ samples, is found to increase progressively with the increasing Ti-content in a sample. A similar trend was noticed in the Sr-doped samples also. However, no significant XRD line shift was noticeable as a result of $Ti^{4+}$ doping at $V^{5+}$ sites, within the limits of experimental error. On the other hand, substitution of Sr at indium sites led to a marginal shift in prominent XRD lines. Overall, the XRD results in Figs. 1 and 2 are indicative of some substitution-induced lattice distortion, while the doped samples retained their basic interconnected chain-like structure and the parental orthorhombic symmetry. The Rietveld analysis of our powder XRD data matched well with the lattice structure and the atomic positions reported for $InVO_4$ by Touboul and Toledano [16]. The typical values in case of $InVO_4$ were found to be: $a = 5.7639$ (3) Å, $b = 8.5337$ (4) Å, $c = 6.5889$ Å.

## Optical properties

The UV–visible spectrum of pure $InVO_4$ was comprised of two intense overlapping peaks in UV region (~250, 320 nm), in addition to a wide visible light (350–700 nm) absorbance band (Fig. 3, curve a). These features match well with the earlier reported UV–visible spectrum of $InVO_4$ [6, 7, 12, 20]. In general, the UV-absorbance remained unaffected on doping at either of the lattice sites.

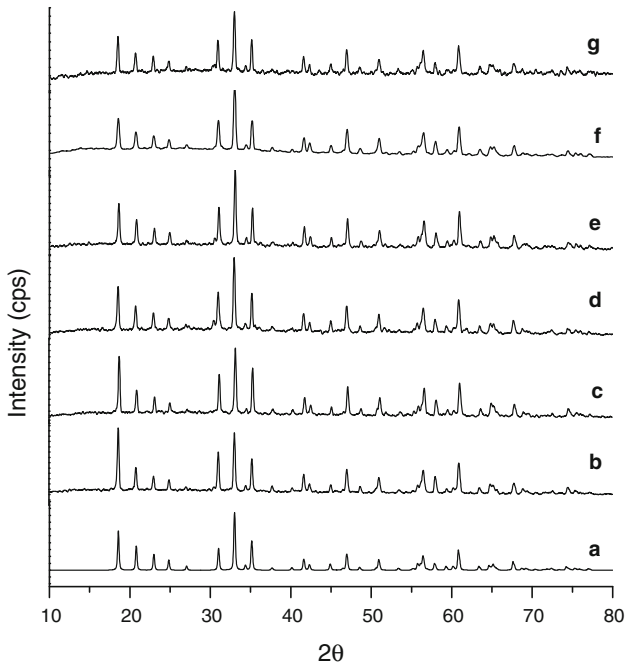


**Fig. 1** Powder XRD patterns of $InVO_4$ photocatalysts with substitution at different lattice sites: (*a*) $InVO_4$ simulated pattern, (*b*) $InVO_4$, (*c*) $InV_{0.98}Ti_{0.02}O_4$, (*d*) $InV_{0.95}Ti_{0.05}O_4$, (*e*) $InV_{0.9}Ti_{0.1}O_4$, (*f*) $In_{0.9}Sr_{0.1}VO_4$, (*g*) $InVO_{1-y}S_y$

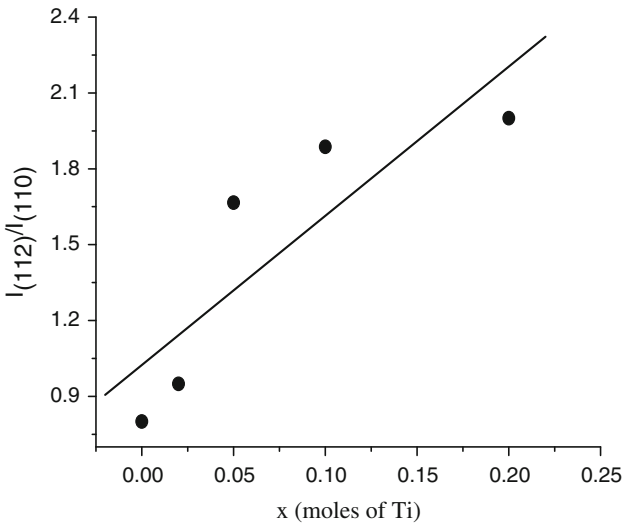


**Fig. 2** The intensity ratio of two prominent reflections of $InV_{1-x}Ti_xO_4$ at $2\theta = 18.56$ and 33.01° ($I_{(1120}/I_{(1100)}$ as a function of Ti content

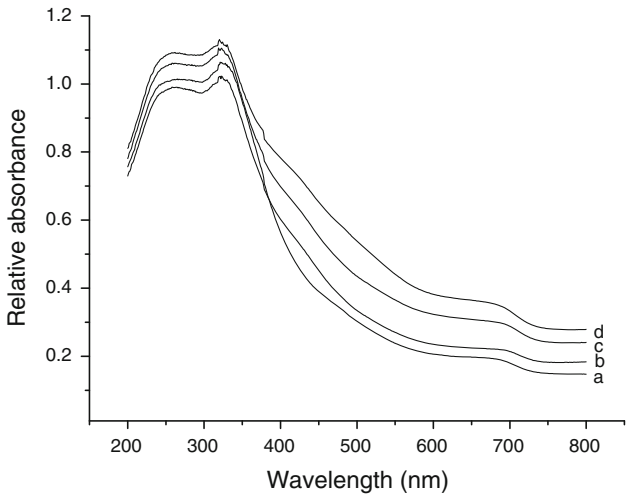


**Fig. 3** UV–visible diffuse reflectance spectra of $InV_{1-x}Ti_xO_4$ photocatalysts as a function of Ti-content. $x$ value: (*a*) 0, (*b*) 0.02, (*c*) 0.05, (*d*) 0.1

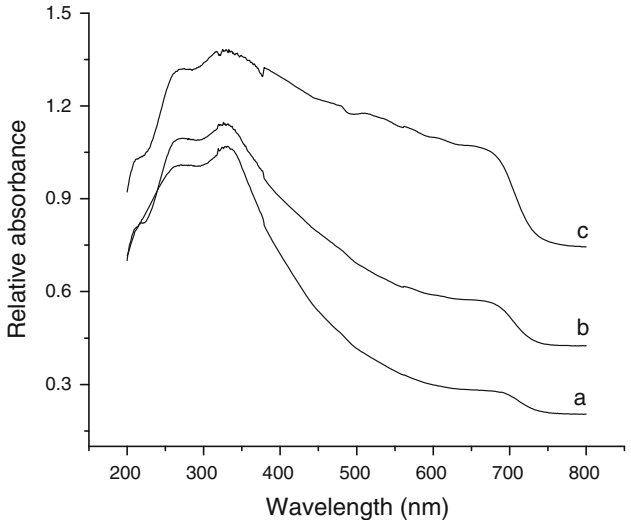


**Fig. 4** UV–visible spectra of S-doped $InVO_4$ samples. (*a*) $InVO_4$, (*b*) $InVO_{1-z}S_z$, (*c*) $InVO_{1-y}S_y$

On the other hand, the intensity of visible region absorption was found to increase considerably, particularly on substitution at either V or at O sites, and also on the dispersion of a metal co-catalyst. Thus, the incorporation of Ti at V sites gave rise to a progressive red shift in the absorption edge (spectra b–d, Fig. 3). Almost similar effect was observed for doping of S at the oxygen sites, the intensity of visible region absorbance increasing drastically even for the trace amounts of sulphur doped. Comparative UV–visible spectra of $InVO_4$ and the two S-doped samples synthesized in this study are presented in Fig. 4. In contrast to the results described above, no significant doping-dependent changes were noticeable for $In_{1-x}Sr_xVO_4$ photocatalysts. Figure 5

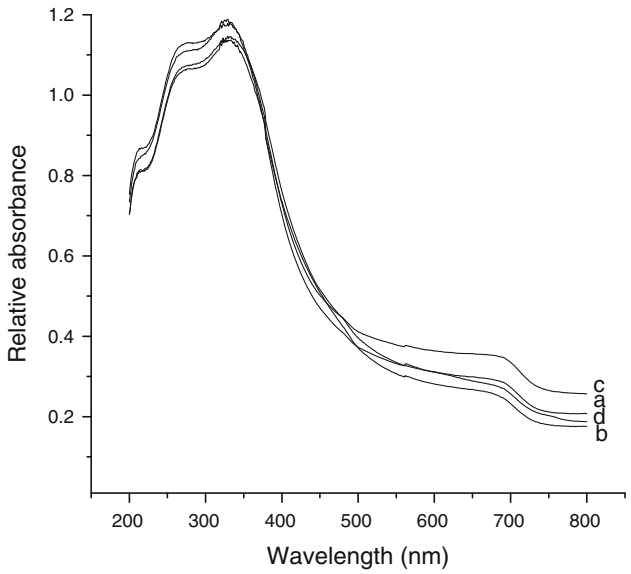


**Fig. 5** UV–visible spectra of $In_xSr_{1-x}VO_4$ samples for $x = 0.02$ (*a*), 0.05 (*b*) and 0.1 (*c*). (*d*) is comparative spectrum of $InVO_4$

presents the comparative UV–visible spectra of different Sr-doped samples. UV–visible spectra of co-catalyst containing samples also displayed an increased intensity of the visible region absorbance (not shown), with no measurable change in UV region (200–400 nm) absorption, for the experiments conducted using pure as well as doped indium vanadate samples. The energy gap at absorption edge of Ti- and Sr-doped photocatalysts, as estimated from the onset in DR UV–vis spectra in Fig. 3, is listed in Table 1.

Figure 6 depicts the room temperature photoluminescence (PL) emission spectra of $InVO_4$ for excitation at different wavelengths. The emission occurred in a broad 350–550 nm region with several overriding fluorescence peaks, centred at ca. 420, 450, 460 and 485 nm. Whereas the nature of this emission spectrum remained the same, the intensity of the emission bands was found to decrease progressively with the increasing excitation wavelength, as is shown in curves (b)–(e) of Fig. 6. Further, almost similar blue-green region PL spectra were observed for the doped as well as the co-catalyst containing samples, with considerable changes in the relative intensity of above-mentioned bands.

## XPS study

Figure 7 shows core level In 3*d*, V 2*p* and O1*s* spectra of $InV_{1-x}Ti_xO_4$ samples for the values of $x = 0$, 0.05 and 0.1. The In $3d_{5/2}$ and In $3d_{1/2}$ XPS peaks of un-substituted indium vanadate were observed at 444.5 and 452.0 eV (curve a, Fig. 7A). These symmetric peaks with a separation of 7.6 eV correspond to 3+ oxidation state of indium [21, 22]. A progressive shift to lower binding energy was

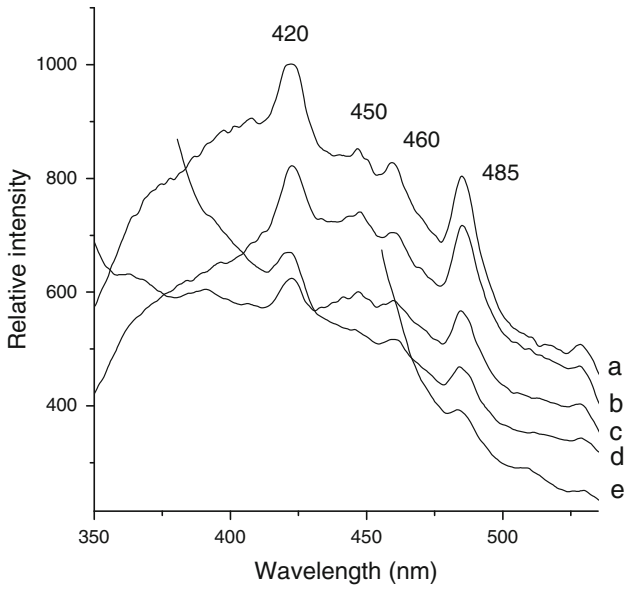


**Fig. 6** Photoluminescence emission spectrum of $InVO_4$ for excitation at (*a*) 280 nm, (*b*) 300 nm, (*c*) 325 nm, (*d*) 350 nm, (*e*) 425 nm

observed in In 3*d* peaks as a result of Ti substitution, with no significant change in peak width (curves b, c Fig. 7A). The spin–orbit components V $2p_{3/2}$ and V $2p_{1/2}$ appeared at 517.0 and 524.5 eV, respectively, corresponding to the $V^{5+}$ oxidation state [21]. The V 2*p* signals were broader in the case of Ti-doped samples; the full width at half maximum (FWHM) increasing from 1.8 eV for $x = 0$ to a value of 2.2 eV for $x = 0.1$. The BE shift in V 2*p* signals was rather small ($\sim$0.2 eV, Fig. 7B). These results indicate again some distortion in the vanadate groups on Ti substitution, without significant change in the oxidation state. We may mention that similar shift of In 3*d* and V 2*p* core levels and the broadening of V 2*p* band have been reported for Li-inserted $InVO_4$ films [21].

The O 1*s* spectra, shown in Fig. 7C, could be de-convoluted into two Gaussian shape peaks, centred at around 530.0 and 531.3 eV. No specific changes in the relative intensity of O 1*s* signals were detectable due to Ti-substitution. The asymmetry of O 1*s* peak on its higher binding energy side is generally ascribed to surface hydroxyl groups [23]. Accordingly, whereas 531.3 eV O 1*s* peak is assigned to the surface hydroxyl groups, 530.0 eV signal is attributable to lattice oxygen. It is pertinent to mention that a similar trend of BE shift and peak broadening was detectable in the Sr-doped samples also.

The XPS spectra of dispersed metals (not shown) revealed the presence of $Au^0$, $Pt^0$ and $Ni^{2+}$ oxidation states. Thus, the XPS spectrum of nickel containing $InVO_4$ displayed a multi-peak Ni 2*p* photoemission spectrum with $2p_{3/2}$ and $2p_{1/2}$ lines appearing at 854.0 and 872.0 eV along with broad satellite peaks at 860.8 and 878.7 eV, a

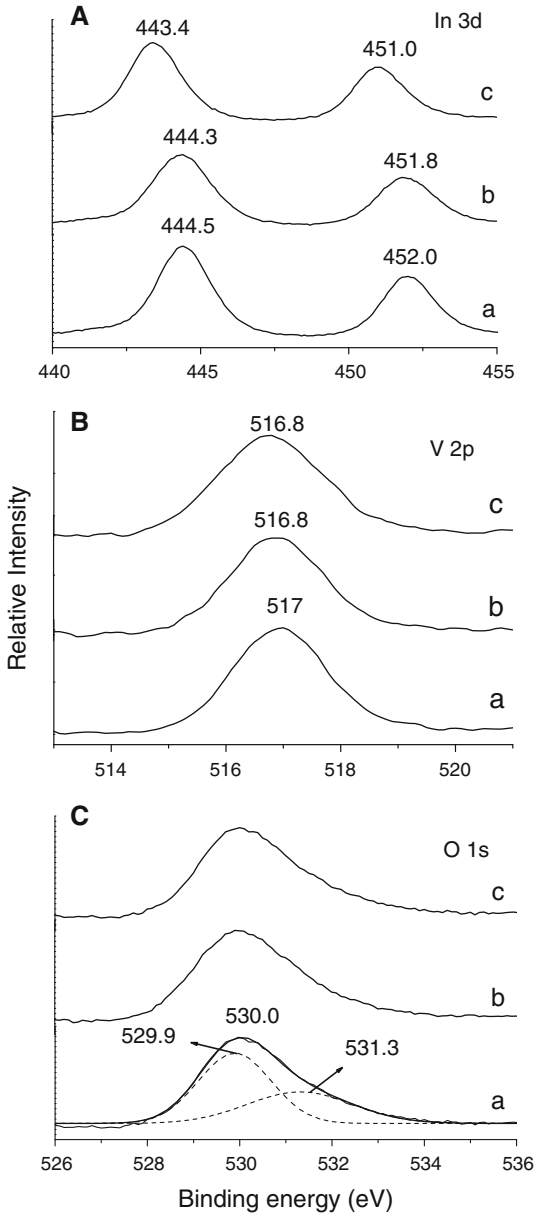


**Fig. 7** Core level In 3*d* (**A**), V 2*p* (**B**) and O 1*s* (**C**) XPS spectra of $InV_{1-x}Ti_xO_4$ photocatalysts as a function of Ti-content. *x* value: (*a*) 0, (*b*) 0.05, (*c*) 0.1

characteristic feature of stoichiometric NiO [24]. The XPS spectrum of gold exhibited symmetric $4f_{7/2}$ (84.0 eV) and $4f_{5/2}$ (87.6 eV) lines corresponding to gold metal and similarly the overlapping Pt $4f_{7/2}$ (71.0 eV) and $4f_{5/2}$ (74.5 eV) peaks were characteristic of zerovalent platinum [22].

## Catalytic activity

Only oxygen and no hydrogen evolution were observed in our experiments when the water suspension of as-synthesized indium vanadates, both pure and impurity doped, were exposed to visible light (>395 nm) for the durations

of up to ~28 h under the experimental conditions of this study. A similar trend was noticed for the samples impregnated with a metal co-catalyst, such as Pt, Ni and Au. The yield of $O_2$, however, depended considerably on impurity content, dispersed metal and the use of a sacrificial reagent, as described below. We may mention that no photolytic reaction occurred in the parallel experiments when pure water and a water/methanol solution were exposed to visible light in the absence of a catalyst. Similarly, no hydrogen was produced when pure water was exposed to prolonged UV irradiation.

The amount of oxygen evolved was rather small during visible light irradiation of pure water in the presence of $InVO_4$ or the co-catalyst containing samples. In these experiments, conducted with no methanol addition, a measurable activity was observed only after an induction period of ~2 h. Subsequently, $O_2$ continued to evolve over a period of several hours, the yield being marginally higher in the case of metal containing samples. Curves (a) and (b) in Fig. 8 show the time-dependent production of $O_2$ using $InVO_4$ and $Pt/InVO_4$ photocatalysts, respectively. The evolution of $O_2$ was almost instant and considerably higher yields were obtained during the irradiation of water/methanol solution in presence of a photocatalyst, $O_2$ yield being higher for the metal containing samples. Curves (c) and (d) in Fig. 8 display oxygen evolution as a function of time, when water/methanol solution was exposed to visible light in the presence of $InVO_4$ and $Pt/InVO_4$ photocatalysts, respectively. As shown in curves (c) and (d), the rate of oxygen evolution is quite high initially and it stabilizes after a lapse of ca. 6–7 h (Fig. 8d). In order to ascertain that the production of $O_2$ occurred as a result of photocatalytic process, the activity measurement was conducted over 2–3 cycles, when the reactor was flushed with $N_2$ at the end of a test run and the experiments was continued on the next day without adding any more photocatalyst or methanol. Again, the oxygen was found to be the only reaction product, even though the reaction rate decreased considerably during the successive test runs.

The yield of oxygen was normally lower for doped $InVO_4$ samples. Comparative data on the rate of $O_2$ evolution using different catalysts (for a test run of ~6 h), all containing a comparable loading (~0.7 wt%) of Pt are presented in Fig. 9. A considerable loss of catalyst activity was observed for the samples doped with ~10 atom% of Ti or Sr (Fig. 9). Further, no significant change in catalytic activity was observed in case of S-doped samples (Fig. 9), in spite of considerable increase in the visible region absorbance (Fig. 4). The indium vanadate samples containing other metal cocatalysts exhibited somewhat lower activity, the trend being: $Pt/InVO_4$ (285 μmol $h^{-1}g^{-1}$) > $NiO/InVO_4$ (110.0 μmol $h^{-1}g^{-1}$) > $Au/InVO_4$ (80.0 μmol $h^{-1}g^{-1}$), where the numbers in the parentheses represent average rate of oxygen evolution, recorded over 6–7 h under Xe lamp irradiation. Similar results, with the activity variation of ca. 5–10%, were observed when the experiments were conducted on several batches of some identically prepared photocatalysts, so as to check for the consistency.

In contrast to the results presented above, small quantities of $H_2$ but no $O_2$ were produced when the metal/$InVO_4$ photocatalysts dispersed in pure water (no methanol) were subjected to UV (250–400 nm) irradiation. The average

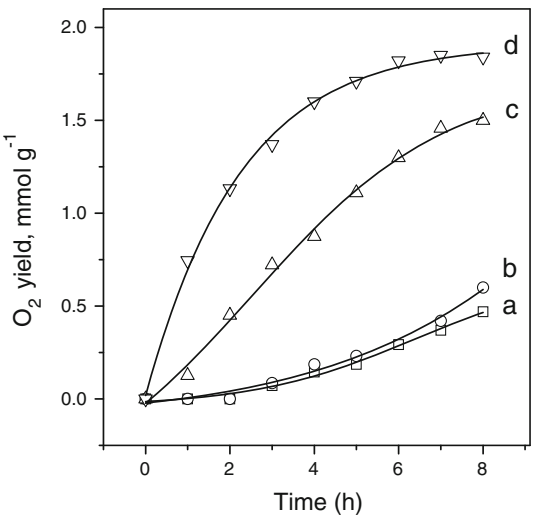


**Fig. 8** Evolution of oxygen as a function of time when pure water (*a*, *b*) and water/methanol solution (*c*, *d*) were irradiated with visible light (>395 nm) in the presence of $InVO_4$ (*a*, *c*) and $Pt/InVO_4$ (*b*, *d*) photocatalysts

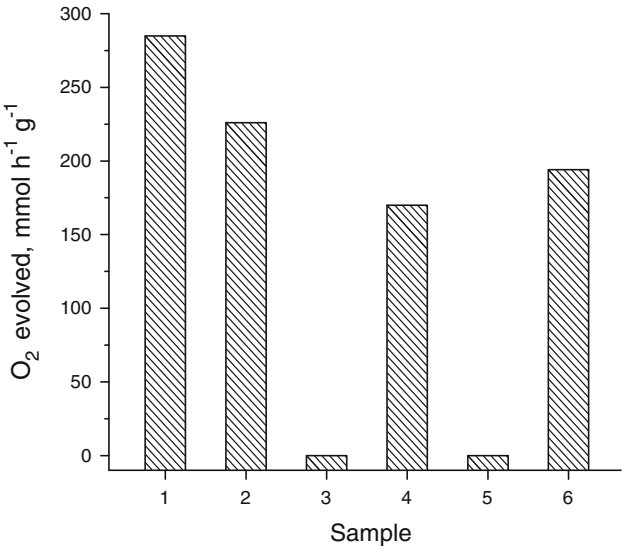


**Fig. 9** Comparative visible-light-induced activity of impurity-doped $InVO_4$ (each containing ~0.7 wt% of dispersed Pt) for the photocatalytic evolution of $O_2$ from water/methanol solution. *1* $InVO_4$, *2* $In_{0.98}Sr_{0.02}VO_4$, *3* $In_{0.9}Sr_{0.1}VO_4$, *4* $InV_{0.98}Ti_{0.02}O_4$, *5* $InV_{0.9}Ti_{0.1}O_4$, *6* $InVO_{1-y}S_y$

rate of $H_2$ evolution in these experiments was ca. 15–25 μmol $g^{-1}$ $h^{-1}$ at the end of a typical ~7 h test run, and varied marginally for different metal cocatalysts dispersed over $InVO_4$. When some representative experiments were conducted by changing the medium pH to ~2 or 14 on adding a few drops of either $H_2SO_4$ or NaOH, no measurable amounts of $H_2$ or $O_2$ could be detected during the UV irradiation of 5–6 h.

## Discussion

The results presented in this paper differ on many counts from several earlier publications on the particulate photocatalytic activity of indium orthovanadate. Thus, contrary to earlier findings [6–8, 12], no measurable amounts of hydrogen were produced in our experiments during the visible-light-induced photocatalytic dissociation of water using $InVO_4$, without or with loading of a co-catalyst (Pt, Au, NiO). We observed PL emission spectra for the excitation at 280–425 nm wavelengths (Fig. 6), in deviation from some other studies [10, 20]. Our energy gap results (Table 1) also differ from the band gap results reported earlier for $InVO_4$ (Table 2). On the other hand, our activity data are in harmony with a recent study [10], where no hydrogen was produced during photoelectrochemical splitting of water using $InVO_4$ and $InVO_4/TlVO_4$ composites. The selective production of oxygen, as shown in Figs. 8 and 9, is in fact akin to the photocatalytic properties of several metal vanadates, e.g. $BiVO_4$, $AgVO_3$ and $Ag_3VO_4$, recorded under visible light irradiation [25, 26].

Since the XRD patterns in Fig. 1 match completely with those reported for $InVO_4$ [6, 9, 13, 20, JCPDS card # 71-1689], it is imperative that the discrepancies mentioned above are not accountable to the crystal structure differences in the samples employed in different studies. Also, the wide variation in the reported band gap of $InVO_4$ (Table 2) bears no direct relationship with the sample morphology and hence the quantum size effects. Thus, a hydrothermally prepared $InVO_4$, with an average particle size of 30–40 nm, is found to exhibit a band gap of ~1.8 eV [8], compared to a band gap of 1.8–2.1 eV for the samples prepared by solid-state method and containing larger size particles [6, 11–13]. On the other hand, $InVO_4$ prepared by a facile aqueous solution method and comprising of 10–30 nm size particles is reported to have a band gap of 3.5 eV [10].

The above described photochemical and photocatalytic properties can, in fact, be interpreted in consideration of the crystal structure and the doping-dependent band characteristics of $InVO_4$. As is documented [16], the lattice of indium orthovanadate contains $InO_6$ octahedra connected to each other by sharing of edges that form chains along [001] direction and are linked together by $VO_4$ tetrahedra. The indium vanadate structure contains rather isolated $VO_4^{3-}$ groups because of a larger V–V distance (4.05 Å), compared to an In–In distance of 3.3 Å [27]. As per the molecular orbital diagram of vanadate ion ($VO_4^{3-}$), the HOMO to LUMO excitation originates from ligand-to-metal charge transfer (LMCT) transition, corresponding excitation energy being ~4.5 eV (~275 nm). When $VO_4^{3-}$ anion is combined with a cation so as to form a crystalline solid, the energy of charge transfer excitation decreases. The extent of this decrease depends upon the nature of the cation [27]. The UV absorption bands in Figs. 3, 4 and 5 may thus be ascribed to absorption in the vanadyl group, and accordingly a value of ~3.1–3.5 eV for its band gap appears to be more appropriate, as is also pointed out in a recent study [10]. This also agrees with the estimated theoretical band gap of $InVO_4$ (Table 2). The

**Table 2** A comparison of band gap values reported for Indium orthovanadate ($InVO_4$)

| S. No | Band gap (eV) | Sample preparation details[a] | Reference |
|---|---|---|---|
| Experimental measurements based on the inflection point in DR UV–visible spectra | | | |
| 1. | 3.5 | A facile solution method (100 °C, 24 h) | [10] |
| 2. | 2.1 | Solid-state reaction (850 °C, 12 h) | [11] |
| 3. | 1.8 | Thin film, solid-state reaction (850 °C, 12 h) | [6] |
| 4. | 1.9 | Solid-state reaction (850 °C, 12 h) | [12] |
| 5. | 1.98–1.90 | A heteronuclear complex as precursor (600, 2–10 h) | [9] |
| 6. | 1.8 | Template-directing self assembling (600–900 °C, 6 h) | [8] |
| 7. | 1.9 | Solid state reaction (825 °C, 2 days) | [13] |
| Theoretical calculation | | | |
| 1. | 3.14 | Density functional theory | [10] |
| 2. | 3.1 | First principal calculation | [14] |
| 3. | 2.3 | DFT calculation | [9] |

[a] Data in the *parentheses* indicate the temperature and the duration of calcination

fact that the substitution at either of the cation or anion position does not affect absorption bands in UV region (Figs. 3, 4, 5), it is apparent that the doping has little effect on the symmetry of the isolated vanadyl group or on the $InVO_4$ lattice structure. This is in harmony with the powder XRD results shown in Fig. 1. The visible region absorbance, on the other hand, is quite sensitive to doping at both the V and the O sites (Figs. 3, 4), and may thus be attributed to the perturbations in vanadyl groups (Figs. 2, 7). These perturbations give rise to certain inter-band donor or acceptor states, close to either the valence or the conduction band. Such localized states and the tentative excitation and relaxation transitions involving the sub-band energy levels are shown schematically in Fig. 10B. The symmetry of $VO_4$ tetrahedra and the V–O bond characteristics in $InVO_4$ are indeed known to vary on doping and also with the sample preparation method [21, 28], in support with our view point.

The doping of an impurity in a mixed metal oxide, such as $InVO_4$, is known to result in significant lattice distortion and hence the creation of various point defects, such as the oxygen ion vacancies and the interstitial sites, depending upon the ionic radius and the valence state of the doped impurity [29]. As is well documented [30], the dopant ions with a valence lower than that of the replaced cation may give rise to an increased concentration of oxygen ion vacancies, so as to maintain the charge neutrality of the host lattice. Accordingly, the substitution of two $V^{5+}$ ions by $Ti^{4+}$ will lead to one oxygen ion vacancy, as per the following expression:

$$2V^{5+} + O_0 \rightarrow 2Ti^{4+} + V_0^{++} + 1/2\,O_2(g) \qquad (2)$$

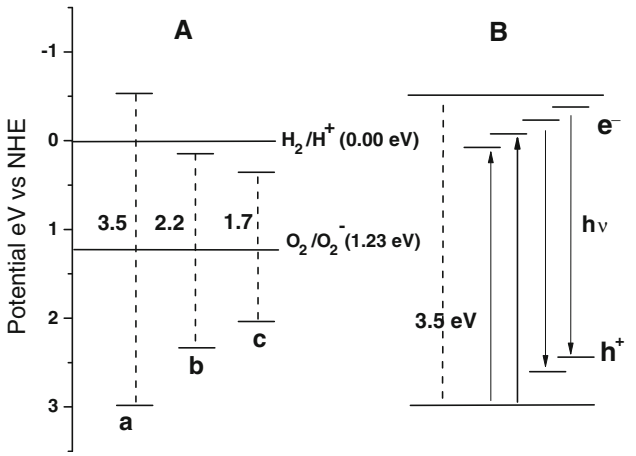


**Fig. 10** A schematic diagram showing: **A** band potentials of $InVO_4$ by Butler–Ginley [18] method for the three tentative band-to-band energy gaps of 3.5 eV (*a*), 2.2 eV (*b*) and 1.7 eV (*c*); and **B** certain closely spaced inter-band charge trapping states and transition energies responsible to visible region absorbance and luminescence emission

where $V_0^{++}$ is the oxygen vacancy with two effective positive charges and the symbol $O_0$ represents an oxygen site with a zero effective charge. As discussed in our earlier publication [31], the doping-induced lattice distortion, as evident from our XRD (Fig. 2) and XPS results (Fig. 7) the oxygen ion vacancies as per the expression 2, and certain inherent lattice defects such as cation vacancies and interstitial defect states, may give rise to certain closely spaced localized charge trapping states, with their energies lying in between the valence and the conduction band of a wide-gap semiconducting metal oxide. Additionally, the aliovalent impurity ions may independently serve as certain donor or acceptor sites to maintain the charge neutrality of host lattice. For instance, whereas dopant $Ti^{4+}$ and $Sr^{2+}$ ions may serve as charge acceptor defect states just above the valence band, the positively charged oxygen vacancies ($V_0^{++}$) would act as electron trapping states, as depicted in Fig. 10B schematically.

The PL spectra in Fig. 6 are in support with our contention. Generally, the luminescence emission in visible region is attributed to the impurities and the structural defects in the wide gap metal oxides [32, 33]. Accordingly, the overlapping luminescence emission bands in Fig. 6 may represent certain discreet energy levels, where the radiative recombination of $e^-/h^+$ charge pair would give rise to visible light emission, as depicted schematically in Fig. 10. Similar luminescence peaks have been attributed earlier to the energy levels produced by oxygen vacancies in $In_2O_3$, caused during sample annealing [34]. The thermoluminescence studies [35] have indeed revealed the existence of such trapping centres in metal orthovanadates, caused by the defects in anionic sub-lattice and also the presence of certain micro-impurities [35]. Since these TL glow peaks are observed at rather low temperatures (<280 K) [35], it is imperative that they arise from certain shallow trapping levels in the close vicinity of valence or conduction band.

The lack of hydrogen formation under visible light (Figs. 8, 9) can thus be rationalized by taking into consideration the energy-gap-dependent band potentials of $InVO_4$, as estimated by using expression 1, and presented schematically in Fig. 10A for the three tentative band-to-band energy gaps. As seen in this figure, the conduction band potential of $InVO_4$ is located at a positive value in respect to the reduction potential of $H^+$ to $H_2$ for the band gap value of less than $\sim$3.0 eV. It is therefore unviable to achieve visible-light-induced hydrogen production from water splitting, as is claimed in several earlier reports [6–8]. The conduction band potential becomes negative (ca. −0.5 eV) for a band gap of >3.2 eV [10], thus making the $H_2$ evolution possible only under UV light, notwithstanding the expected changes in band potentials as a

function of pH and also the additional energy requirement because of the possible bending of individual bands. The evolution of small amounts of hydrogen has indeed been noticed in our experiments conducted over metal/$InVO_4$ under UV light, as mentioned above. The visible region absorbance (Figs. 3, 4, 5) and the evolution of $O_2$ as shown in Figs. 8, 9 may thus relate to the inter-band energy levels, shown schematically in Fig. 10B. These attributes are in general agreement with the recent photo-electrochemical investigations on $InVO_4$ [10, 36]. As proposed by Enache et al. [36], the UV–visible spectra in Figs. 3, 4 and 5 may represent two distinct energy regimes, one corresponding to band-to-band energy-gap of 3.2–3.5 eV, and another due to sub-band gap transitions giving rise to absorption at lower energies (<3.2 eV). In tune with our inferences, the low energy absorption of $InVO_4$ has been ascribed to sub-band gap transitions in Ref. [36]. Further, our flat band potential calculations (Fig. 10A) are also corroborated by the photo-electrochemical measurements in [36], reporting a small value of −0.04 V with respect to reversible hydrogen electrode for a band-to-band energy gap of 3.2 eV, and that too at a solution pH of 13.6. For an energy gap of 3.5 eV, the conduction band potential has been reported to be lower than that of hydrogen electrode [10]. This substantiates our observation that $InVO_4$ may assist in water splitting only under UV-irradiation, and supports the activity trend observed in Figs. 8 and 9. Our study also reveals that the doping-induced microstructural lattice defects and the resultant sub-band charge trapping states (Fig. 10B) may play an important role in the overall photocatalytic properties of a metal oxide system, as has been brought out in our earlier study on this subject [31].

The observed enhancement in $O_2$ yield on methanol addition is against the well reported role of methanol as an electron donor or hole scavenger [37]. In our opinion, the alternative role of $CH_3OH$ can be understood by invoking the primary steps involved in semiconductor-mediated photocatalytic decomposition of water into $H_2$ and $O_2$ [38], viz.

1. In semiconductor:

$$\text{Photocatalyst} + h\nu \rightarrow 2e^- + 2h^+ \quad (3)$$

2. In water:

$$H_2O \rightarrow OH^- + H^+ \quad (4)$$

The overall reaction:

$$2e^- + 2H^+ \rightarrow H_2 \quad (5)$$

$$2h + 2OH^- \rightarrow 2H^+ + 1/2\,O_2 \quad (6)$$

We envisage that the function of a sacrificial reagent may not confine to its selective interaction with one of the photo-generated charge carriers (step 3) to minimize the $e^-/h^+$ recombination. Instead, the organic compounds, such as $CH_3OH$, may also interact with the ionic species in step 4, thus controlling the final reaction products (steps 5, 6). Various possible ion–radical-controlled reaction steps in the semiconductor-mediated photooxidation of methanol have been enumerated in our earlier study [39]. The above described activity results of our study, e.g. smaller induction periods for oxygen evolution from methanol/water solution, lowering of reaction rate with increasing time (Fig. 8) and the progressively decreasing $O_2$ yields during successive test runs, indeed point to the direct participation of methanol molecules in photocatalytic reaction, as is the case for other sacrificial reagents such as silver nitrate.

A similar activity trend observed by using different co-catalysts, such as $Pt^0$, $Au^0$ and $Ni^{2+}$, indicates that the role of a dispersed metal is to provide some distinct binding sites at the metal/oxide interfaces for the adsorption of water molecules and their subsequent interaction with photo-generated charge carriers. The metal-dependant variation in the rate of oxygen evolution, as mentioned above, may depend upon the size and the morphology of dispersed metal particles and also the interfacial characteristics of metal/oxide heterojunctions. These aspects have been dealt with in more detail elsewhere [40, 41].

## Conclusions

Following are the important findings of this study:

1. Indium vanadates, without and with doping of an impurity at its lattice sites are found to serve as efficient photocatalysts for visible-light-induced photooxidation of water. The rate of $O_2$ evolution increased considerably on dispersion of a metal co-catalyst, and also on addition of methanol as sacrificial reagent. The samples having high impurity content exhibited poor photocatalytic activity.
2. The $InVO_4$ samples gave rise to blue-green photoluminescence emission spectrum, with several overlapping bands at ca. 420, 450, 460 and 485 nm, on excitation at wavelengths in 250–420 nm range. Whereas the intensity of these emission bands decreased progressively with increasing excitation wavelength, their relative intensity was found to depend on the impurity content.
3. Powder XRD, luminescence and XPS results revealed that the doping of an impurity, particularly at V or O sites, give rise to distortion in $InVO_4$ lattice in addition to creation of oxygen ion vacancies.

4. The microstructural lattice defects, arising from the aliovalent lattice substitutions, give rise to certain inter-band charge trapping states. The preferential entrapment of charge carriers at these trapping states may in turn play a crucial role in deciding the optical, photochemical and photocatalytic properties of a semiconducting metal oxide.
5. The position of absorption edge in UV–visible spectra is quite sensitive to above-mentioned lattice defects, and may not necessarily represent the true band-to-band energy gap of a wide gap metal oxide. Accordingly, the energy values of <3.0 eV, projected earlier as band gap of $InVO_4$ (Table 2), may in fact correspond to the energy transitions in-between the closely spaced sub-band trapping states (Fig. 10B).

**Acknowledgements** Authors thank the Department of Science and Technology (SERC, DST), New Delhi, for the financial support to this research project. The help of Dr K.R. Patil in XPS study is gratefully acknowledged. The reviewers are thanked for their valued comments.

## References

1. Sahaym U, Norton MG (2008) J Mater Sci 43:5395. doi:10.1007/s10853-008-2749-0
2. Van de Krol R, Liang Y, Schoonman J (2008) J Mater Chem 18:2311
3. Stroyuk AL, Kryukov AI, Kuchmii SY, Pokhodenko VD (2009) Theor Exp Chem 45:209
4. Osterloh FE (2008) Chem Mater 20:35
5. Kudo A, Miseki Y (2009) Chem Soc Rev 38:253
6. Lin HY, Chen YF, Chen YW (2007) Int J Hydrogen Energy 32:86
7. Ye J, Zou Z, Arakawa H, Oshikiri M, Shimoda M, Matsushita A, Shishido T (2002) J Photochem Photobiol A 148:79
8. Lixian X, Lixia S, Chongfang M, Yuanwei L, Feng W, Qunwei L, Hongxing D, Hong H, Jihong S (2006) Chin J Catal 27:100
9. Zhang L, Fu H, Zhang C, Zhu Y (2006) J Solid State Chem 179:804
10. Butcher DP, Gewirth AA (2010) Chem Mater 22:2555
11. Ge L, Xu M, Fang H (2006) J Sol-Gel Sci Technol 40:65
12. Ye J, Zou Z, Oshikiri M, Matsushita M, Shimoda M, Imai M, Shishido T (2002) Chem Phys Lett 356:221
13. Zou Z, Arakawa H (2003) J Photochem Photobiol A 158:145
14. Oshikiri M, Boero M, Ye J, Aryasetiawan F, Kido G (2003) Thin Solid Films 445:168
15. Randeniya LK, Murphy AB, Plumb IC (2008) J Mater Sci 43:1389. doi:10.1007/s10853-007-2309-z
16. Touboul M, Toledano P (1980) Acta Crystallogr B 36:240
17. Klug HP, Alexander LE (1974) X-ray diffraction procedures: for polycrystalline and amorphous materials, 2nd edn. Wiley, New York, p 618
18. Butler MA, Ginley DS (1978) J Electrochem Soc 125:228
19. Xu Y, Schoonen MAA (2000) Am Miner 85:543
20. Li Y, Cao M, Feng L (2009) Langmuir 25:1705
21. Cimino N, Artuso F, Decker F, Orel B, Vuk AS, Zanoni R (2003) Solid State Ion 165:89
22. Wagner CD, Riggs WM, Davis LE, Moulder JF, Muilenberg GE, Briggs D (1979) Handbook of X-ray photoelectron spectroscopy. Perkin Elmer Corporation, USA
23. Natile MM, Glisenti A (2002) Chem Mater 14:3090
24. Kim KS, Davis RE (1972–1973) J Electron Spectrosc 1:251
25. Konta R, Kato H, Kobayashi H, Kudo A (2003) Phys Chem Chem Phys 5:3061
26. Kudo A, Omori K, Kato H (1999) J Am Chem Soc 121:11459
27. Dolgos MR, Paraskos AM, Stolzfus MW, Yarnell SC, Woodward PM (2009) J Solid State Chem 182:1964
28. Gotić M, Musić S, Ivanda M, Šoufek M, Popović S (2005) J Mol Struct 744–747:535
29. Kröger FA (1974) The chemistry of the imperfect crystals. North Holland, Amsterdam, p 207
30. Kumari N, Krupanidhi SB, Varma KBR (2010) J Mater Sci Mater Electron 21:1107
31. Shah P, Bhange DS, Deshpande AS, Kulkarni MS, Gupta NM (2009) Mater Chem Phys 117:399
32. Liang CH, Meng GW, Lei Y, Philipp F, Zhang LD (2001) Adv Mater 13:1330
33. Chen SJ, Liu YC, Shao CL, Mu R, Lu YM, Zhang JY, Shen DZ, Fan XW (2005) Adv Mater 17:586
34. George PP, Gedanken A (2008) Eur J Inorg Chem 6:919
35. Khodos MYa, Fotiev AA, Shulgin BV (1974) Izvestia Akademii Nauk SSSR Neorganicheskie Materialy 10:1658
36. Enache CS, Lloyd D, Damen MR, Schoonman J, Van de Krol R (2009) J Phys Chem C 113:19351
37. Hara M, Hitoki G, Takata T, Kondo JN, Kobayashi H, Domen K (2003) Catal Today 78:555
38. Zou Z, Ye J, Arakawa H (2003) Int J Hydrogen Energy 28:663
39. Bhattacharyya K, Varma S, Kumar D, Tripathi AK, Gupta NM (2005) J Nanosci Nanotechnol 5:797
40. Malwadkar SS, Gholap RS, Awate SV, Korake PV, Chaskar MG, Gupta NM (2009) J Photochem Photobiol A 203:24
41. Awate AV, Sahu RK, Kadgaonkar MD, Kumar R, Gupta NM (2009) Catal Today 141:144